COMET: a new end-station at SOLEIL for coherent magnetic scattering in transmission

H. Popescu, J. Perron, B. Pilette, R. Vacheresse, V. Pinty, R. Gaudemer, Maurizio Sacchi, R. Delaunay, F. Fortuna, K. Medjoubi, et al.

To cite this version:

H. Popescu, J. Perron, B. Pilette, R. Vacheresse, V. Pinty, et al.. COMET: a new end-station at SOLEIL for coherent magnetic scattering in transmission. Journal of Synchrotron Radiation, 2019, 26 (1), pp.280-290. 10.1107/S1600577518016612 . hal-02106187

COMET a new end-station at SOLEIL for coherent magnetic scattering in transmission

H. Popescu[1], J. Perron[1,2], B. Pilette[2], R. Vacheresse[2], V. Pinty[1], M. Sacchi[1,3],

R. Delaunay[2], F. Fortuna[4], K. Medjubi[1], R. Gaudemer[1], J. Luning[2] and N. Jaouen[1]

[1] Synchrotron SOLEIL, Saint-Aubin, B.P. 48, 91192 Gif-sur-Yvette, France
[2] LCP-MR, UMR 7614, CNRS-UPMC, rue P. et M. Curie, 75005 Paris, France
[3] INSP, UMR 7855, CNRS-UPMC, 4 Pl. Jussieu, 75005 Paris, France
[4] CSNSM, Université Paris-Sud, Bât. 104, 91405 Orsay, France

Abstract: *We have developed and built a new instrument, named* ***COMET for CO****herent* ***M****agnetic scattering* ***E****xperiments in* ***T****ransmission, using polarized soft X-rays. This high-vacuumset-up is placed at the intermediate focal point of the elastic branch of the SEXTANTS beamline at Soleil. The main application is in solid state physics, the instrument being optimized for studying material propertie using coherent scattering of soft X-rays with an emphasis on imaging, with chemical selectivity, the magnetic domains of artificially nano-structured materials. The instrument principal features are presented and illustrated through recently performed experiments.*

1. Introduction:

The magnetic materials have a very important role in key technologies like information handling (storage, logic and sensor devices), high power gigahertz nano-oscillators or high performance magnets for motors. Nano-magnetism is therefore a very promising research topic. In order to understand the fundamental magnetic properties of the matter, powerful characterization techniques and tools are needed. Macroscopic information, like the average magnetization over a large volume, is often not sufficient to understand the local microscopic details. For this, one needs high resolution imaging of the magnetic nano structures with the possibility to record the evolution of the system at different timescales ranging from ns down to fs. Thus many magnetic imaging techniques have been developed, like scanning probe (MFM), electron probe (TEM) or photon probe. In the photon probe category we can distinguish techniques based on the optical microscopy (Kerr and Faraday) and on the use of polarized X-rays. The new instrument presented in this paper is part of this last category. x-rays or X-ray, always the same.

Soft x-rays cover the binding energies of the 1s electrons in carbon, oxygen and nitrogen and the 2p electrons of transition metals like Fe, Co and Ni and 3d electrons in rare earth metals. The wavelength ranges between ~0.5 and ~10 nm, making soft x-rays a proper tool for imaging nanoscale structures. The polarization properties of soft x-rays play a crucial role for the study of the magnetic materials. The specific interaction of polarized x-rays with magnetic matter gives rise to various dichroism effects. X-rays magnetic circular dichroism (XMCD) is the difference in absorption of left and right circularly polarized light when the photon energy is tuned to an absorption edge of a given element. This effect is proportional to the projection of the magnetic moment of the element onto the photon propagation direction. XMCD is adapted to the study of ferromagnetic and ferrimagnetic materials. The x-rays magnetic linear dichroism (XMLD) is the difference in absorption of linearly polarized photons between the polarization parallel and perpendicular to the magnetization axis. XMLD, related to the spatial anisotropy of the squared magnetization, can be observed in both ferromagnetic and anti-ferromagnetic materials, but such measurements are more often applied to the study of the latter.

In the following we will give a brief overview of different techniques and existing instruments dedicated to magnetic imaging with polarized soft x-rays, which we classify in two main categories: using x-ray optics and lens-less imaging.

For the soft x-ray regime the refractive index is close to unity, thus imaging with conventional lenses is impossible. This limitation was overcome in the 80s with the development of the nanolithography where a new type of lens was developed: the Fresnel zone plate (FZP). This is a diffractive optics, typically circular gratings, where the line density is increasing from the center in the radial direction, while keeping constant the wavelength difference between neighboring lines. The performance of a FZP, i.e. the spatial resolution that can be obtained and the focal point, is determined by the number of zones and the width of the outermost zone [D. Attwood, Soft X-Rays and extreme Ultraviolet Radiation. Cambridge, U.K.: Cambridge Univ. Press, 1999]. Two different imaging techniques can be done using FZP optics: full-field transmission soft x-ray microscope (TXM) and scanning transmission soft x-ray microscope (STXM). In a TXM full-field microscope the FZP forms a complete image of the sample at the 2D detector, typically a CCD camera. One example is the XM-1 x-ray microscope at the Advanced Light Source (ALS) in Berkeley. The spatial resolution that can be attained is around 25 nm for around 15 microns of field of view. Obtaining a complete real space image can take few seconds only.

Differently, a STXM uses the FZP to focus monochromatic radiation to a small spot on the sample. An image is obtained by scanning the sample across the focus spot of the FZP. The transmitted photons can be recorded with fast point detectors. One example is the MAXYMUS(M?) microscope in BESSY II (Berlin) [http://www.helmholtz-berlin.de], reporting resolutions below 20 nm.

Both TXM and STXM are routinely used for imaging the magnetic structures in transmission, where the detected signal contains thickness averaged information. The STXM microscope makes it possible to form an image using detection modes other than transmission, for instance photoelectron and fluorescence emission, widening the range of application to non-transparent samples.

A complementary approach to provide only surface sensitivity is the X-PEEM [A. Scholl, “Applications of photoemission electron microscopy (PEEM) in magnetism research”, Current Opinion Solid State Mater. Sci., vol. 7, no. 1, pp. 59-66, 2003.], which is a hybrid between an x-ray source and a high resolution electron microscope. The emission of secondary electrons from the sample is proportional to the x-ray absorption. Only the electrons from the first few nm can escape the sample, making XPEEM a surface sensitive magnetic imaging technique. As an example, a leading instrument is PEEM3 at ALS with a spatial resolution down to 20 nm [https://als.lbl.gov/beamlines/11-0-1].

The lensless imaging approach is using the coherent scattering of soft x-rays in resonant conditions and requires a high degree of longitudinal and transverse coherence. These imaging techniques can be classified in two main parts: x-ray holography techniques, based on the interference between the main beam and a reference beam, and imaging techniques based on retrieval algorithms (ex. ptychography). For the holography technique a simple Fourier inversion of the diffraction diagram is reconstructing the real space image. The new COMET instrument, described in this paper, is based on these lensless techniques for imaging magnetic structures.

The SEXTANTS beamline [1] at Soleil is dedicated to the use of resonant scattering of polarized soft x-rays, implementing several techniques as Resonant inelastic X-ray scattering, diffraction, reflectivity and coherent scattering, with four specialized experimental end-stations open to users: AERHA [2], RESOXS [3], IRMA [4] and the new one here presented, COMET. The photon energy range covered by the beamline is from 50 eV to 1700 eV, with full control of polarization (linear horizontal, vertical or custom, and circular left or right). The flux at the sample position for the different stations exceeds 10^{12} photons/sec over the optimized 100-1000 eV energy range.

The COMET instrument is placed at the intermediate focal point of the elastic branch of the SEXTANTS beamline (figure 1). COMET has been designed to have an easy beam switch between this instrument and the KB end-station placed downstream on the same elastic branch of the beamline. Two differential pumping blocks, placed upstream and downstream from the COMET instrument, ensure fast beam availability, downstream and upstream, after venting. Typically, after one hour of pumping, the pressure in the main chamber enters the 10-6 mbar range, which is enough in order to open towards the rest of the beamline.

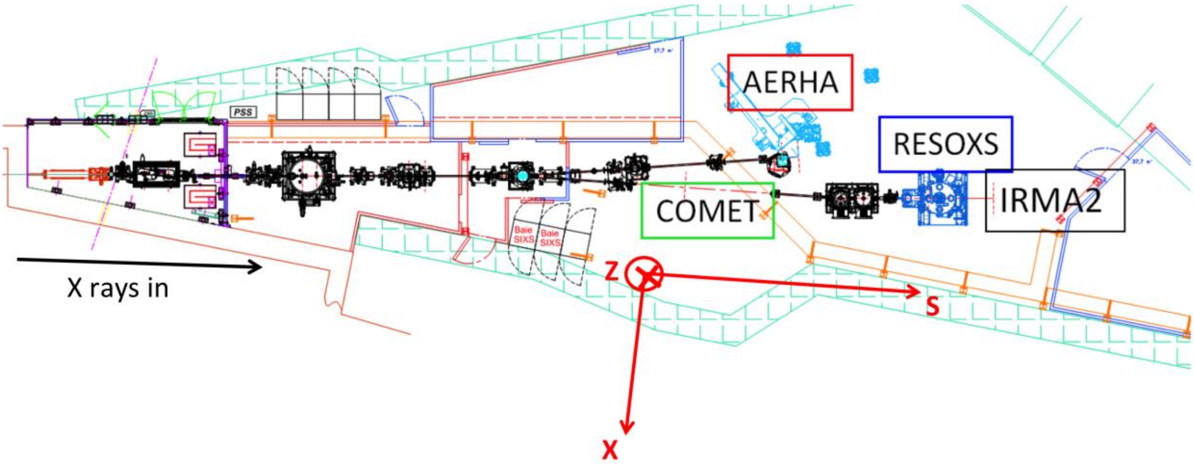

Figure 1: Top view schematics of the SEXTANTS beamline, with the four experimental end-stations: AERHA on the inelastic branch, and COMET (intermediate focal point), RESOXS and IRMA2 (KB focal point) end-stations on the elastic branch. In the standard Soleil coordinate system, the S direction in along the beam and the X direction perpendicular to the beam, in the horizontal plane. Z (not shown here) is the vertical direction.

2. Instrument design

2.1 Vacuum chambers

This station has been designed to have a very high mechanical stability(?). Two main vessels compose this instrument: the sample environment and the 2D detector ones, placed on the same marble table. The sample chamber (cubic) has removable flanges with double viton gaskets (figure 2), primary pumped in between. The periphery flanges are standard CF40 and CF63, for regular electric and fluid feed-throughs and for view-ports. The lateral rectangular flange is a two point quick access door, for easy sample exchange and set-up pre-alignment while vented. The modular removable walls permit later upgrades of the chamber. The typical pressure available in user operation is between 10^{-6} to 10^{-7} mbars. Part of this instrument was developed in collaboration between SOLEIL and the LCPMR team [Sorbonne University, Paris, France].

The 2D detector chamber (cylindrical) has only CF flanges and is isolated from the main chamber by a CF150 gate valve. It remains under vacuum for very long periods allowing a base pressure of 10^{-7} mbar despite the presence of the CCD detector and cabling. These chambers have turbo pumps equipped with rubber covered bellows for vibration damping.

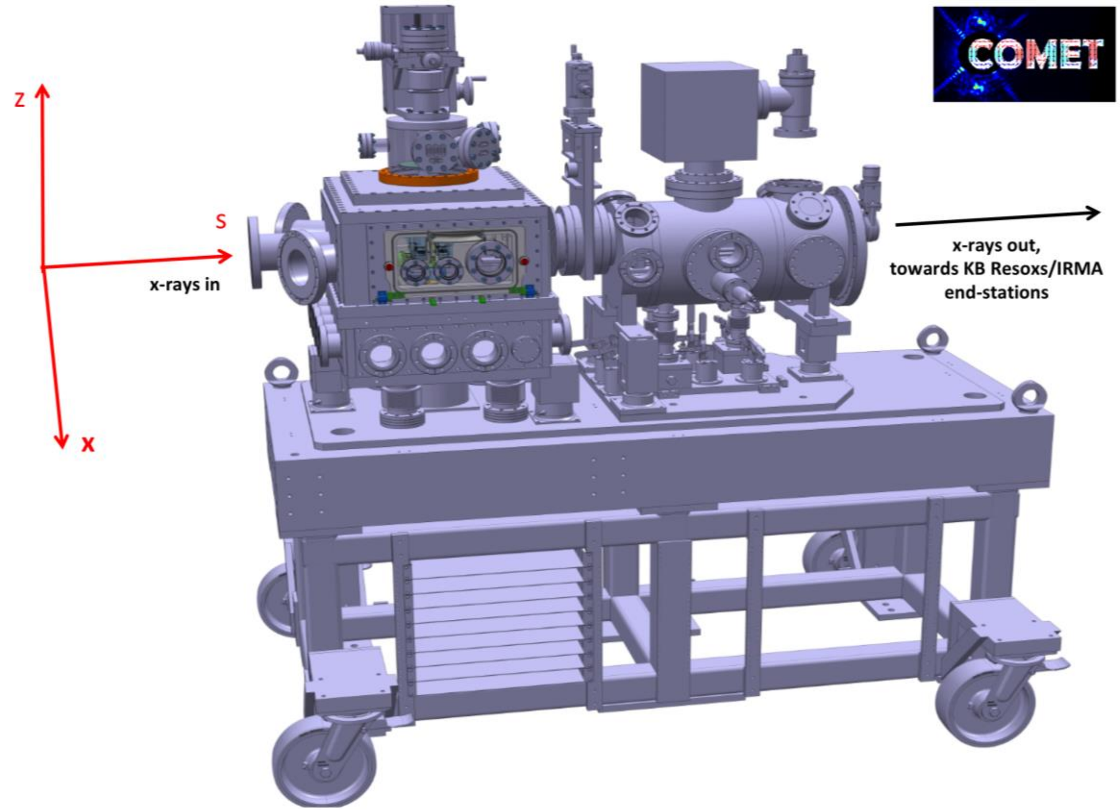

Figure 2: COMET chamber, with the cubic sample vessel on the left and the CCD vessel on the right.

2.2 Beam conditioning

The spatial (transverse) coherence at the sample is directly related to the angular acceptance of the beamline. The coherence of the SEXTANTS beamline was measured [4] using Non Redundant Apertures (NRA). While the vertical coherence distance is naturally ensured by the vertical small size of the beam even in full acceptance mode, for the horizontal coherence the beamline front-end slits have to be reduced. At 700 eV the transverse coherence distance obtained is better than 25 x 25 µm^2, with a remaining current of monochromatic and coherent beam of around 1 µA measured using an AXUV-100 diode (from Opto Diode Corp, USA), corresponding to 10^{10} coherent and monochromatic ($R \approx 10^4$)? 700 eV photons per second arriving at the sample of the COMET instrument.

A piezoelectric shutter is placed just behind the exit slits of the monochromator, where the beam has a vertical size that depends on the slit opening, typically between 30 and 50 microns. The shutter is composed by a 4 cm long piezo blade, driven by high voltage, which can bend vertically by several hundred microns, ensuring a complete blanking of the beam. The open/close states are trigged directly by the CCD controller, with a minimum response time around 10 ms. During acquisitions, this device blocks the x-ray beam while reading out the detector.

2.3 Sample positioner

The optical table inside the sample chamber is directly mounted on a synthetic marble, through stable columns. The flexible bellows around these columns permit vibration damping from the pumping system.

Several under vacuum motorized blocks (figure 3) compose the sample environment, in the beam arrival order:

1) Guard-hole: An XZ piezo stage [SmarAct, Germany], holding different pinholes for cleaning the incoming beam and choosing the precise illuminated region on the sample (typically few tens of microns). The travel in each direction is 21 mm, with encoded positioning to 500 nm resolution. The high quality pinholes are fabricated by focused ion beam (FIB) using the facility operated by the CSNSM team.

2) Mask: An SXZ piezo stage (SmarAct) with the same parameters as the ones previously described. These masks are used for FTH (Fourier Transform Holography) imaging technique [8], in the separated mask and sample approach [9, 10, 11], or for ptychography experiments [12]. Both techniques require a very small distance between the mask and the sample, ranging from contact to 1 mm, depending on the experiment. In the case of contact mode, for the separated mask and sample approach in holography, the parallelism between the mask and the sample is done by autocollimation using the synchrotron white beam. The mask and the sample are parallel to each other when the visible light reflected by either one is sent back through the same path of the incoming light. For this aligning procedure the mask holder is equipped with two supplementary manual rotations (shown in figure 3 under the mask piezo block).

3) Sample a): a high load stepper motor SXZ bloc [PI-MiCos, Germany], with 35 mm travel in each direction and 150 nm encoded resolution is holding the sample. The high load makes it possible to install a variety of sample environments, like electromagnetic coils, cooling stripes, RF feed-throughs, etc.

Sample b): An additional piezo SXZ block (SmarAct), with 31 mm travel and 50 nm encoded resolution can be added for high resolution scans, dedicated to the ptychography experiments. Two miniaturized piezo rotation encoded stages (SmarAct) are available for custom experiments (ex. Tomography) to be developed on User's demand.

4) diode: the 1x1 cm^2 Al capped AXUV-100 diode is placed 15 cm behind the sample for the fine alignment of all the previous elements. This retractable diode is mounted on a horizontal 100 mm travel stage (SmarAct), together with a protection screen for the CCD detector.

5) The mask and sample systems are placed on an intermediate table which can rotate around the Z axis (typically +/- 45°). The table rotation is ensured by a heavy load motorized rotation stage. Figure 3 shows this

intermediate table in two positions: normal incidence (left) and 45° incidence (right). This 45° incidence is useful for getting the projection, for example, of the in-plane magnetic components [14]. In this case we can use for holography either a reference slit [15] or specific angle drilled reference holes [11] for the masks.

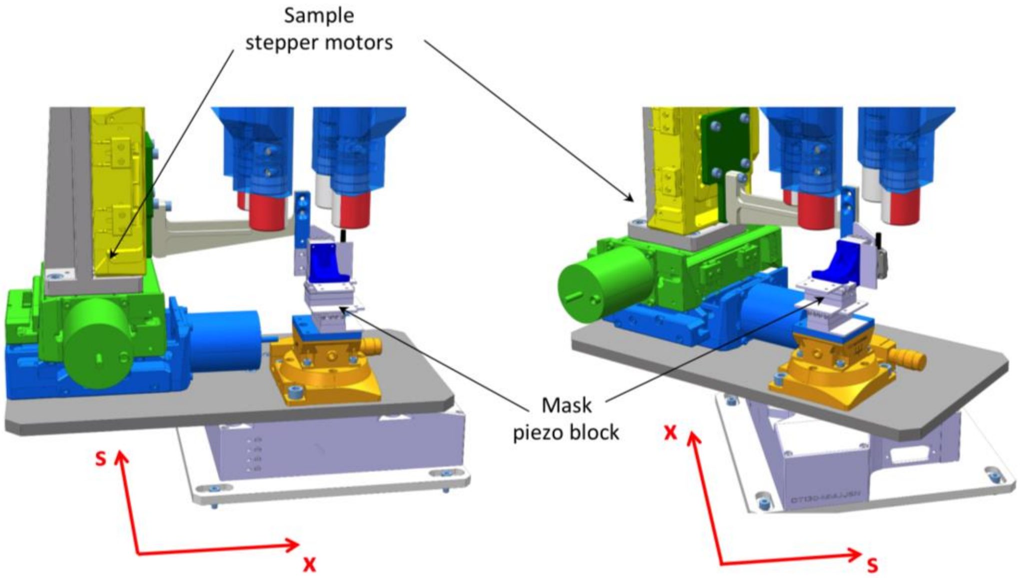

Figure 3: Left: internal mechanics seen from the beam, with the main rotation set for normal incidence. Right: internal mechanics seen from the side, with the main rotation set for 45° incidence. The four rods coming from the top are permanent magnets.

2.4. Sample environment

We developed an environment capable of delivering static magnetic fields of up to 1 Tesla in all the directions in the horizontal plane. The system is based on four rotatable, transversely-magnetized permanent magnet rods [O. Cuget, P. Hansson and J. M. D. Coey, IEEE Transcactions on Magnetics, Vol. 30, No. 6 (1994)].

The four cylindrical permanent magnets (NdFeB rods with 26 mm diameter) have independent under vacuum motorized and encoded rotations (figure 4 a). The diagonal distance between the magnets and the sample (located at the central axis of the four magnetic rods) can be varied by using a mechanical Archimedean spiral system (green part on the 3D representation in figure 4 a) driven by a single stepper motor in order to simultaneously change and keep symmetrically the same gap on the four magnets. All the motors have gear mechanisms with great reduction ratio in order to maintain the considerable torque forces. The combination of the gap and the individual angles permits the tuning of the resulting static field at the sample position to a precise direction and magnitude in the horizontal plane.

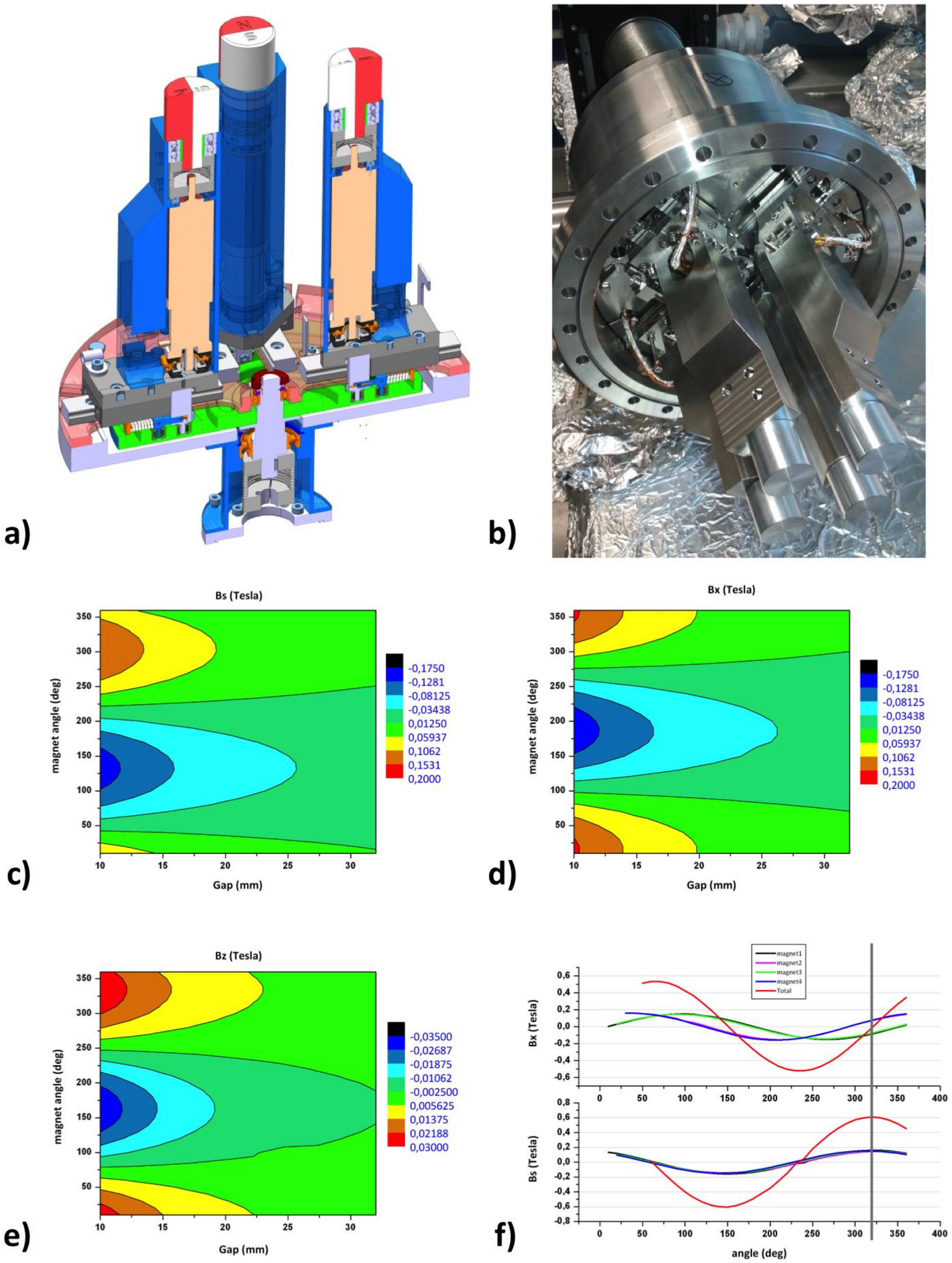

Figure 4. Four permanent magnet system delivering at the sample position (i.e. on the central axis) a total static field of up to 1 Tesla. a): cut over the 3D engineer design. b): real setup, here shown in the commissioning phase. At present this device is installed and available at the COMET end-station (the upper part shown in figure 3). c): magnetic field measured in the s direction (along the beam) for one single magnet. d): magnetic field measured in the x direction (perpendicular to the beam) for one single magnet. e): magnetic field measured in the vertical direction for one single magnet. f): resultant field for the 4

magnets together, matched in order to maximize the field in the s direction while cancelling it in the perpendicular direction.

For the commissioning phase we used a 3D Hall sensor, placed at the sample position, in order to calibrate the magnetic field as a function of the angles and gap for each magnet. We recorded the Bs, Bx and Bz magnetic field intensities as angle/gap maps for each magnet, separately. Figure 4 (c, d and e) shows the measured magnetic field created by a single magnet in the s, x and z directions, respectively.

The resultant field created by the four magnets together is then the vector addition of the individual components. Figure 4f shows the total field resulting from the combination of the four magnets, here with the angles matched in order to maximize the field in the s direction (along the beam), while cancelling the resulting field in the x, perpendicular to the beam, direction. In a similar way, other preferential directions for the resultant field can be obtained in the horizontal plan.

For this commissioning phase the minimum gap measured was limited to 10 mm because of the size of the Hall sensor holder. In normal conditions, without the Hall sensor, the gap can go to 7 mm, corresponding to a maximum field of 1T (the four magnets phased together) at the sample level. In the results chapter we present the example of a real experiment showing the evolution of magnetic domains versus the applied external static field using a test Co/Pd multilayer sample.

The homogeneity of the resultant field is better than 3% within a radius of 2 mm around the center of the four magnets, in the closest gap configuration (the highest gradients). The beam was aligned in the center of the four magnets with a precision better than 0.5 mm by using a mechanical adapter mounted on the magnets and specially designed for this alignment procedure. The standard beam size on the sample is few tens of microns and the imaged fields of view are typically few microns, so we can consider that the field strength is homogenous and well known along the whole imaged area.

The material of the permanent magnets is NdFeB with a remanent field Br = 1.37 Tesla. The field strength changes with the temperature within 0.1% per degree. Since the permanent magnets are not in direct mechanical contact with the sample, they remain close to room temperature and the low/high temperature of the sample is compatible with the high magnetic static field, allowing combined sample environments. This magnetic environment is also compatible with the separate mask and sample approach and with the normal or tilted transmission geometry, as shown in figure 3.

The temperature environment can be controlled via a commercial He cryostat/heater [Janis, USA] ending with a local flexible stripe, the actual temperature on the sample being from 20K to 800K (magnet heating by radiation. The temperature regulation is done via a Lakeshore 350 controller with stability better than 1 mdeg. The temperature environment might not be compatible with the extendable field of view techniques, as the thermic drifts can affect the alignment between the mask and the sample.

RF pumping is also possible via an external RF generator and SMA feedthrough (as shown in results paragraph [18]).

2.5 Detection

The main detector is a 16 bit PI-MTE CCD camera, with 2048 x 2048 pixels. The chip and pixel size are 27.? mm and 13.5 µm respectively. The real dynamic range of the detector goes from 100 counts (background level) to around 20000 counts, this being the maximum value before producing saturation effects.

A movable frame is integrated to the CCD head using a motorized XZ piezo system. The frame travel is 31 mm in both transversal directions, with position encoded to 50 nm resolution (encoded ???). This frame can hold two different spherical beam-stops with typical sizes of few hundred microns, placed at 2 cm in front of the chip. An Al filter (100 nm thick) protects the CCD against the visible light coming mainly from the encoders.

The CCD is mounted on a stable optical table using three columns coupled to the marble (figure 5). The under vacuum CCD carriage is motorized and can slide the CCD along the beam propagation direction (s direction). The travel of the carriage covers a sample-to-CCD distance from = 15 to = 45 cm (z is used elsewhere, no?, and is chosen in order to have the best tradeoff between the pixel size and the field of view of the reconstructed image, both depending on the CCD pixel size and on the number of pixels.

The reconstructed pixel size is directly proportional to the wavelength and to the maximum angular momentum collected by the CCD: λd/2048x13.5µm, where d is the sample to CCD distance. As an example, for the Co edge (778 eV), the theoretical reconstructed pixel size is 9 nm when the CCD is at a distance of 15 cm from the sample, and 26 nm when the CCD is placed at a distance of 45 cm. In reality the size of the reconstructed pixel is defined by the actual spreading of the diffraction diagram within the CCD chip size.

The CCD can also move in x direction (perpendicular to the beam propagation direction), but only in retracted position, with 5 cm travel, in order to let the beam pass through and reach the downstream KB experimental station.

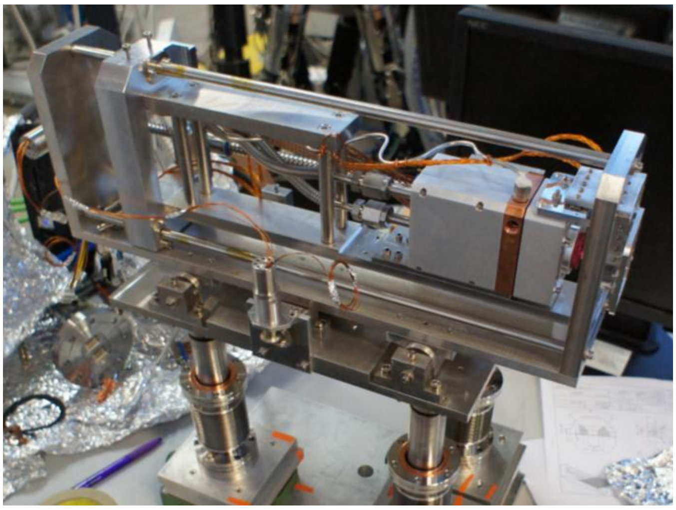

Figure 5: Internal mechanics holding the retractable CCD. The XZ beam-stop and a 100 nm Al filter are integrated to the CCD head.

3. Control Command:

All the motors and detectors are integrated in the SOLEIL standard Tango control system and fully interfaced with the SEXTANTS beamline acquisition software. Automatic scans are possible using the Python environment, depending on the complexity of the experiment.

Multi-dimensional scans, using the CCD as detector, can be used in an automatic mode for ptychography or tomography measurements, where diffraction diagrams are recorded for different (x, z) sample positions, scanned with custom trajectories (spiral, mesh, etc.).

Fast 2D maps (figure 6) can also be done using a scalar detector (the rear diode) coupled to a high sensitivity Keithley 6517 electrometer in order to localize and identify the sample patterns or mask coordinates.

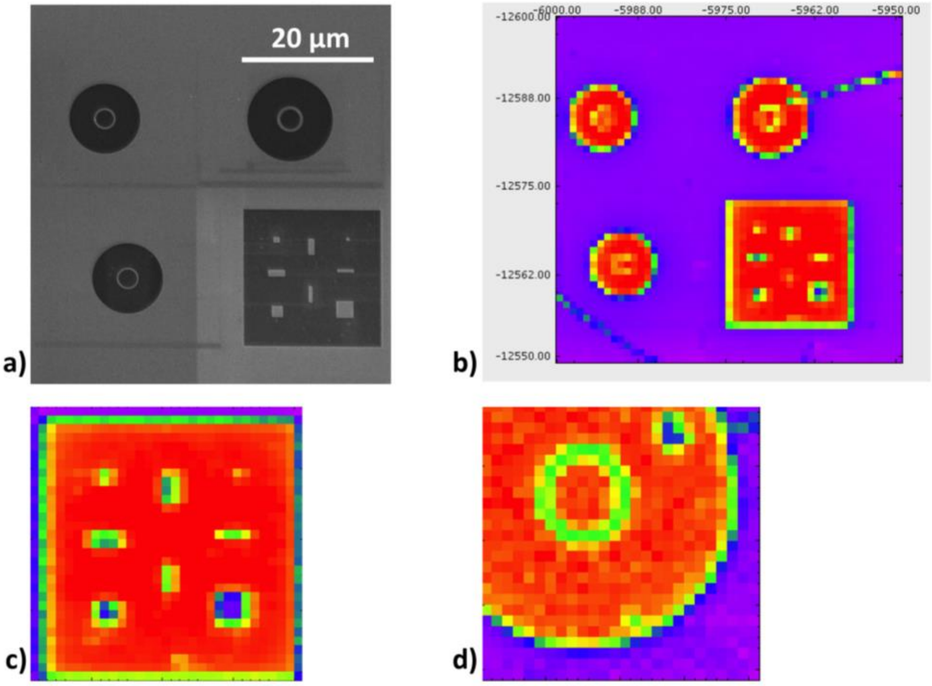

Figure 6: sample fast mapping in order to localize the nano-patterns of interest. a): SEM image of CoPd nano-patterns on Si_3N_4 membrane, taken while FIB milling. The white scale-bar is 20 µm. b): 2D fast mapping of the same sample using the piezo motors and the transmission diode into the Comet chamber. c) and d): zoom on the identified nano-objects.

Photon energy scans can be performed in transmission mode using either the diode (for the integrated signal through the sample) or the 2D detector, in order to get the XAS or the energy-dependent evolution of speckles.

Different communication ports (serial, GPIB, analog voltage in/out, power, etc.) are available and interfaced with the Tango control, for driving and triggering the eventual user custom material, like RF generators, coils, power supplies, etc.

4. First experimental results:

This instrument was commissioned and has already served for a few user experiments. Here the performance of the instrument will be illustrated by a brief description of early results.

4.1 Time resolved holographic imaging in integrated mask and sample approach:

Time resolved experiments were done at Sextants beam-line using the COMET instrument. User custom samples with integrated RF antenna and holography mask permitted to excite a magnetic vortex and image the core displacement as a function of time [18]. The diameter of the holography object aperture was 3.7 microns, and the Co square pattern inside was 2 microns. The sample to CCD distance was 27 cm. The delay between the x-ray pulse and the local magnetic excitation was controlled via a RF generator triggered by the synchrotron clock. These experiments were done either in 45° transmission geometry in order to get the in plane magnetic domains, or at 0° to see the out of plane magnetic components of the domain walls. The holography mask had a slit for encoding the reference beam, and the reconstruction was done using the Heraldo technique [15]. In figure 7 up-left we display a typical diffraction diagram where we can observe the Airy rings from the object hole and the vertical diffraction of the slit. The observed core oscillations have a periodicity of 3.5 ns [18].

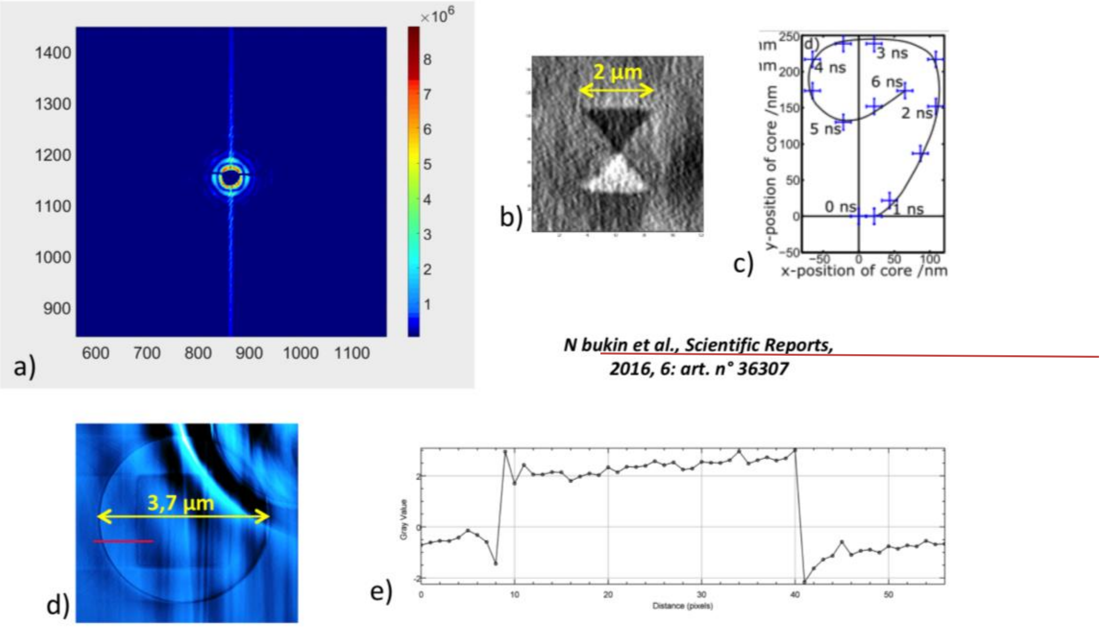

N bukin et al., Scientific Reports,
2016, 6: art. n° 36307

Figure 7. a): diffraction diagram from a sample with integrated slit reference. Axis coordinates are in pixels and the intensity scale-bar in counts. The maximum scattering vector corresponding to the shown diffraction diagram (i.e. at 300 pixels from the direct beam) is $4\pi \sin(\vartheta)/\lambda = 0.112$ nm^{-1}. b): reconstructed magnetic vortex (in plane magnetic component, done at 45° geometry). c): vortex core position versus time. d): charge (non-magnetic?) image of the square. e): intensity profile along the red line in d) for testing the imaging resolution. The intensity change over the topological border takes place within one reconstructed pixel, where the pixel size is 21.7 nm.

In the figure 7 d we show the reconstructed image of the 2 µm Co square (topological part only, obtained by adding the signal from the two helicities) and the intensity profile (figure 7 e) corresponding to the red line crossing the gold mask to the left and the Co square to the right. The measured pixel size is 21.7 nm, calculated from the known size of the square pattern. We observe that the intensity changes when crossing the edges of the FIB defined structures takes place within one pixel, thus we conclude that the spatial resolution of our imaging setup is better than 21.7 nm.

4.2 Holographic imaging of magnetic domains in the integrated mask/sample approach.:

For testing the permanent magnet setup of Fig. 4 we used a 40 repetitions Co/Pd multilayer, with an integrated gold mask for holography. The object hole was 2 microns in diameter. The energy of the circularly polarized photons was tuned to the Co edge (778 777? eV). The individual angles of the four permanent magnets were chosen in order to have a resultant magnetic field oriented normal to the sample surface (s direction, parallel to the beam). The gap was varied from 12 mm (500 mT) to 32 mm (80 mT).

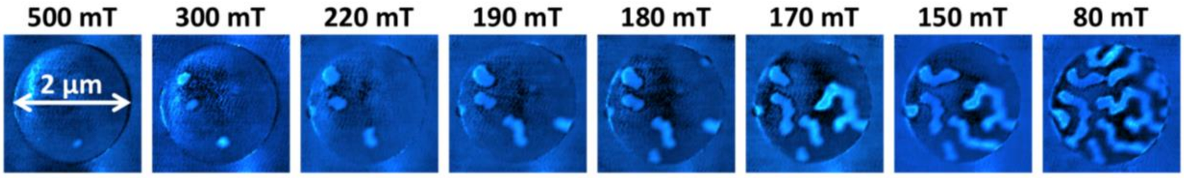

Figure 8: Magnetic domains evolution as a function of the field strength, from few bubble-like domain nucleation (close to saturation) to homogenous worm domains (close to remanence).

figure 8 shows the evolution of the magnetic domains with the strength of the magnetic field applied normal to the Co/Pd layers. These images are purely magnetic (difference of the two photon helicities). At high field values the magnetic layer is almost entirely saturated in the field direction (+s), with only few bubbles still remaining in the opposite direction (-s). While increasing the four magnets gap (i.e. decreasing the magnetic field strength at the sample position) the bubbles start to increase in size until the stable worm-like magnetic domain structure forms below ~100 mT. This is the equilibrium configuration with balanced “up” and “down” magnetic domains that do not evolve much with a further decrease of the field down to remanence.

4.3 Holographic imaging of magnetic domains in the separate mask/sample approach:

Preparing the holography mask and the sample on two separate x-ray transparent membranes allows one to image different parts of the sample, effectively extending the FTH field of view [ref-ref]. For testing this configuration in the COMET setup we used a continuous [Co(0.6nm)/Pt(1nm)]x20 multilayer sample, fabricated at the CNRS-Thales Laboratory [19]. This multilayer shows out of plane bubble-like magnetic domains at ambient temperature and represents a prototype system for skyrmion nucleation [20, 21].

The holography image was done using the separate mask and sample approach, in normal transmission geometry. The x-ray beam energy was tuned to 778 eV (Co L edge), in circular polarization. The mask consisted of a 1.8 µm diameter object hole and three reference holes with diameters around 80 nm.

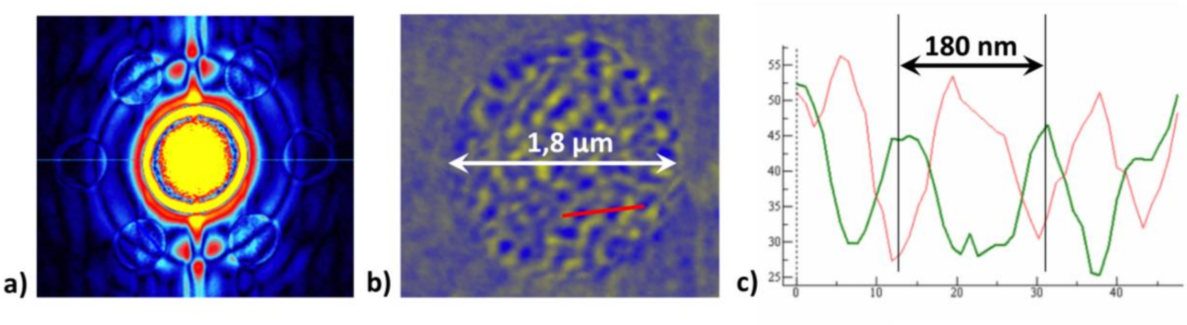

Figure 9: a) Fourier transform of the diffraction diagram, with six cross-correlation images produced by the three references. b) Zoom on one of the cross-correlations showing the magnetic image (subtraction between the two helicities). c) Intensity plot profiles for the two polarizations, separately, over the red line in b).

In figure 9 a) we show the 2D Fourier transform of the diffraction diagram. This corresponds to the square modulus of the autocorrelation of the mask and sample transmission function. The central disk is the autocorrelation of the object beam, while the six satellites are the cross-correlations between the object and the references (each of the three independent cross-correlations is accompanied by its corresponding complex conjugate). As the reference holes are much smaller than the object hole, these cross correlations represent the reconstructed transmission functions of the object, with a resolution given primarily by the size of the corresponding reference hole. The intensity (thus the contrast) of the reconstructed object goes with the size of the reference, being inversely proportional to the resolution.

One of the reconstructed objects from figure 9 a) is zoomed in figure 9b). This is the subtraction between images taken with different circular polarization helicities, thus the shown structures are purely magnetic. The quantitative profiles for the two separate polarizations, corresponding to the red line in figure 9 b) are displayed in figure 9 c) for both polarizations. As expected, they have inverted contrast and we can estimate a magnetic domain size around 90 nm. For this experiment the resolution was imposed by the size of the reference hole, i.e. 80 nm.

5 Ptychography :

The COMET end-station is adapted for the ptychography imaging technique [22], were the sample position is scanned with respect to the incoming coherent beam (the probe) to create a sequential array of overlapping illuminated areas. For each illuminated area, the coherent diffraction pattern is recorded with a 2D detector in the far field region. To reconstruct the phase and the amplitude images, the Extended Ptychography Iterative Engine (EPIE) algorithm [23] is used. An improved ptychographical phase retrieval algorithm for diffractive imaging was implemented by Kadda Medjubi from the Nanoscopium beamline [24] into a Matlab script (The MathWorks, Natick, MA, USA) running on a 132 Gb RAM and 8 core processor personal computer.

A proof of principle experiment was performed on a patterned Co/Pd multilayer (40 repetitions) sample, as used in ref [10], illuminated with a 778 eV coherent beam defined by a 1 µm diameter pinhole. The distance between the pinhole and the sample was several???? hundred microns. The sample to CCD distance was 42 cm, thus the size of the reconstruction pixel was 25 nm.

figure 10 a) and b) show the reconstruction of a 1x3 μm^2 rectangle, done at the Co edge with circular left and right polarizations, respectively. For the sample positioning we used stepper motors with 150 nm encoded resolution. The curves in c) correspond to the intensity line profiles in a) and b). In this case the resolution was 300 nm, and it was measured as the distance corresponding to an intensity variation from 10% to 90% through the blurred edge of the rectangle. The local modulations of the two curves correspond to the magnetic domains and they are perfectly inverted as the images were taken with inverted photon helicities at resonance.

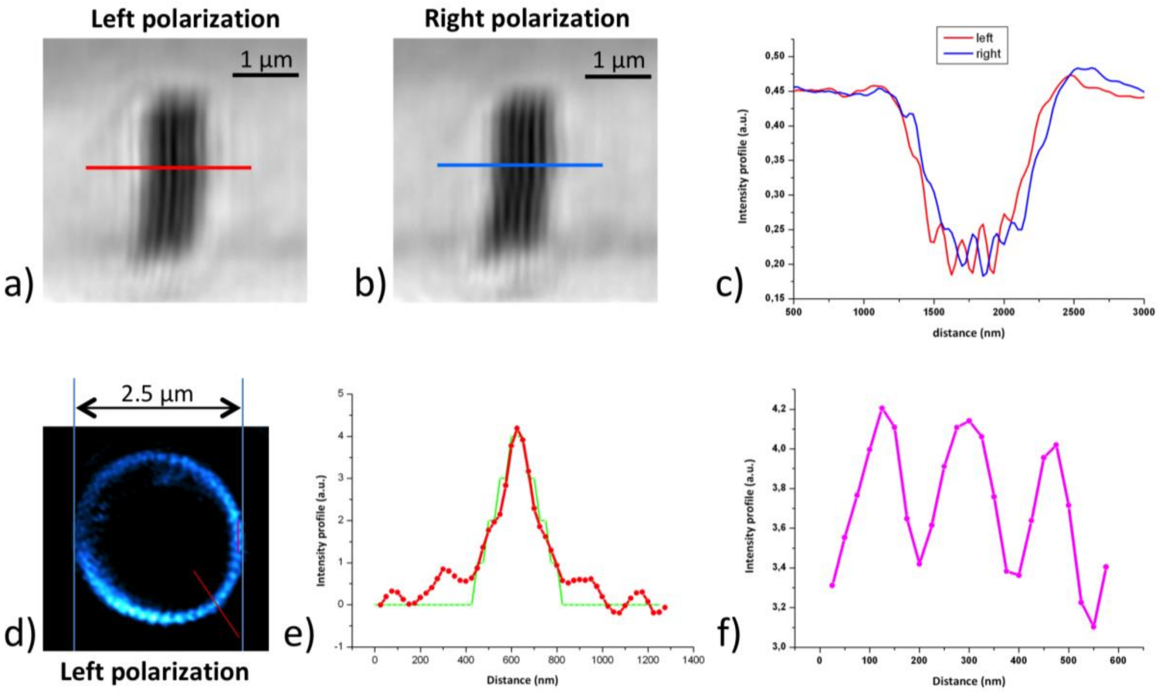

Figure 10: ptychography image reconstruction. a) and b): reconstructed image of a 1x3 µm^2 magnetic pattern done by scanning with stepper motors and using circular polarization, left and right, respectively. c): line profiles of a) and b). d): reconstructed image of a magnetic ring 2.5 microns in diameter and 170 nm wide, done by scanning with piezo motors and using left circular polarization. e): intensity profile along the red line in d) (red curve); the green curve is the convolution between a 170 nm wide box function and a Gaussian of 75 nm sigma radius. This comparison means the experiment resolution was 150 nm. f) Intensity profile along the magenta line in d) showing the contrast generated by the magnetic domains within the ring.

The image in figure 10 d) is the reconstruction of a magnetic ring of 2.5 microns in diameter and 170 nm lateral size. The experiment was done using piezo motors with 50 nm positioning resolution and one micron beam size on the sample. Gaussian blurring with different sigma radius were used on a 170 nm box function in order to compare with the experimental profile. The best fit was for a 75 nm sigma radius (figure 10 e)) thus we can conclude an imaging resolution of 150 nm.

The advantage of this technique is the possibility to image large fields of view without the need to put in contact the sample and the mask, as the case of holography with extended field on view (see 4.3). The final resolution depends on several parameters: the reconstructed pixel size, defined by the maximum scattering vector collected by the detector (in the examples above the reconstructed pixel size was 25 nm), the positioning precision of the sample (50 nm in Fig. 10d), the size of the beam on the sample and the efficiency of the retrieval algorithms. Further improvements can be done, like reducing the sample to detector distance, using nm precision piezo frames and reducing the size of the incident beam (zone plate).

Conclusion:

We have designed and built a new experimental chamber dedicated to soft x-ray coherent diffraction imaging in transmission. This station is already functional at the SEXTANTS beam-line of the SOLEIL Synchrotron and available to the user community. The main applications are in the field of solid-state physics and particularly of magnetic nano-structured materials. The state of the art resolution obtained with our instrument at the SEXTANTS beamline and employing a user custom mask is ~20 nm.

Our instrument is complementary to other existing magnetic imaging microscopes in the world, with some advantages and disadvantages. While the obtained spatial resolutions are about the same, the measuring conditions are different from one instrument to the other. For example a PEEM is dedicated to surface imaging only and is a good candidate for studying non-transparent samples e.g. epitaxially grown on solid substrates, not feasible with the transmission techniques. On the other hand the interaction with the electrons limits the applied external field to few tens of mT. A TXM/STXM works in transmission and allows fast recording of large fields of view, within seconds or tens of seconds, but the radiation dose on the sample can be very high. The focus distance of a zone plate, i.e. the space between the FZP and the sample is typically a few hundreds of microns, limiting the possibilities for the sample environment like coils or RF antennas. The holography in transmission with integrated mask permits high resolution imaging with a variety of experimental conditions applied to the sample, like temperature changes, external magnetic/electric fields or RF pulses. On the other hand the sample fabrication is more complex and the acquisition times are longer compared to STXM.

Thanks to the versatility of the COMET set-up, future developments are underway. For the present CCD, the read-out time in full-chip mode is around 4 seconds, for exposure times generally within half a second per acquisition. This means that the most of the time is actually spent for read-out, thus the development of future high frame-rate detectors is crucial. We planned to install shortly an additional 2D detector of the CMOS type, already successfully tested with soft x-rays, characterized by a much faster read-out time to improve drastically the efficiency of the data collection. Installing a piezo frame with nm positioning precision is also planned for improving the resolution of the ptychography experiments.

Another ongoing project is the setup at the beamline of a fs laser coupled to the x-ray beam to perform pump-probe time resolved experiments. The time structures available at the SOLEIL sychrotron will make it possible to image laser-induced magnetic transitions with time resolutions of either 50-100 ps (standard mode) or 5-10 ps (low-alpha mode ref.)..

Considering the wide energy range available at the SEXTANTS beamline (50-1700eV) we would like to point out that this instrument may also be used for non-magnetic coherent scattering investigations in the soft X-rays range in order to benefit from the absorption edges available in this range, notably C, N and O K-edges.

Acknowledgments:

The authors would like to thank W. Legrand, N. Reyren, V. Cros for providing the Co/Pt multilayer and M. Viret for discussion in the early conception stage of the magnetic device. We wish also like to thank K. Desjardins for his help in the test and commissioning of the CMOS detector.

References:

[1] M. Sacchi, N. Jaouen, H. Popescu, R. Gaudemer, J.M. Tonnerre, S.G. Chiuzbaian, C.F. Hague, A. Delmotte, J.M. Dubuisson, G. Cauchon, B. Lagarde, F. Polack, *The SEXTANTS beamline at SOLEIL: a new facility for elastic, inelastic and coherent scattering of soft X-rays*, J. Phys. Conf. Series, 425, 072018 (2013).

[2] S. G. Chiuzbăian, C. F. Hague, A. Avila, R. Delaunay, N. Jaouen, M. Sacchi, F. Polack, M. Thomasset, B. Lagarde, A. Nicolaou, S. Brignolo, C. Baumier, J. Lüning, and J.-M. Mariot, *Design and performance of AERHA, a high acceptance high resolution soft x-ray spectrometer*, Review of Scientific Instruments 85, 043108 (2014)

[3] N. Jaouen, J. M. Tonnerre, G. Kapoujian, P. Taunier, J. P. Roux, D. Raoux, F. Sirotti, *An apparatus for temperature-dependent soft X-ray resonant magnetic scattering*, J. Synchrotron Rad. 11, 353-357 (2004)

[4] M. Sacchi, H. Popescu, R. Gaudemer, N. Jaouen, A. Avila, R. Delaunay, F. Fortuna, U. Maier and C. Spezzani, *IRMA-2 at SOLEIL: a set-up for magnetic and coherent scattering of polarized soft x-rays* , Journal of Physics: Conference Series, Volume 425, Part 20

[5] http://www.lcpmr.upmc.fr

[6] https://www.photonicsonline.com/doc/absolute-x-ray-photodiode-ird-axuv-100gx-0001

[7] http://www.smaract.de

[8] S. Eisebitt, J. Lüning, W. Schlotter, M. Lörgen, O. Hellwig, W. Eberhardt, J. Stöhr, *Lensless imaging of magnetic nanostructures by x-ray spectro-holography*, Nature 432, 885–888 (2004).

[9] C. Tieg, R. Frömter, D. Stickler, H. Stillrich, C. Menk, S. Streit-Nierobisch, L-M Stadler, C. Gutt, O. Leupold, M. Sprung, G. Grübel and H. P. Oepen, *Overcoming the field-of-view restrictions in soft x-ray holographic imaging*, J. Phys.: Conf. Ser. 211, 012024 (2010).

[10] C. Spezzani, F. Fortuna, R. Delaunay, H. Popescu, and M. Sacchi, *X-ray holographic imaging of magnetic order in patterned Co/Pd multilayers*, Phys. Rev. B 88, 224420 (2013).

[11] H. Popescu, F. Fortuna, R. Delaunay, C. Spezzani, V. López-Flores, N. Jaouen, M. Sacchi, *Four-state magnetic configuration in a tri-layer asymmetric ring*, Appl. Phys. Lett. 107, 202404 (2015).

[12] J. R. Fienup, *"Phase retrieval algorithms: a comparison."*, Applied Optics 21 (15): 2758–2769 (1982).

[13] http://www.pimicos.com

[14] C. Tieg, R. Froemter, D. Stickler, S. Hankemeier, A. Kobs, S. Streit-Nierobisch, C. Gutt, G. Gruebel and H. P. Oepen, "*Imaging the in-plane magnetization in a Co microstructure by Fourier transform holography*", Opt. Express, 18, 27251 (2010).

[15] T. A. Duckworth, F. Ogrin, S. S. Dhesi, S. Langridge, A. Whiteside, T. Moore, G. Beutier, and G. van der Laan, *Magnetic imaging by x-ray holography using extended references*, Opt. Express 19, 16223-16228 (2011).

[16] https://www.janis.com

[17] https://www.lakeshore.com/products/Cryogenic-Temperature-Controllers

[18] N. Bukin, C. McKeever, E. Burgos-Parra, P.S. Keatley, R.J. Hicken, F.Y. Ogrin, G. Beutier, M. Dupraz, H. Popescu, N. Jaouen, F. Yakhou-Harris, S.A. Cavill, G. van der Laan, *Time-resolved imaging of magnetic vortex dynamics using holography with extended reference autocorrelation by linear differential operator*, Sci Rep. 2016 Oct 31,6:36307.

[19] http://www.cnrs-thales.fr

[20] J.-Y. Chauleau, W. Legrand, N. Reyren, D. Maccariello, S. Collin, H. Popescu, K. Bouzehouane, V. Cros, N. Jaouen, and A. Fert, *Chirality in Magnetic Multilayers Probed by the Symmetry and the Amplitude of Dichroism in X-Ray Resonant Magnetic Scattering*, Phys. Rev. Lett. 120, 037202 (2018)

[21] J.-Y. Chauleau, W. Legrand, N. Reyren, D. Maccariello, S. Collin, H. Popescu, K. Bouzehouane, V. Cros, N. Jaouen, A. Fert, *Chirality in magnetic multilayers probed by the symmetry and the amplitude of dichroism in X-ray resonant magnetic scattering*, arXiv:1709.08352 (2017).

[22] F. Pfeiffer, *X-ray ptychography*, Nature Photonics 12, 9-17 (2018)

[23] A. M. Maiden & J.M. Rodenburg, *An improved ptychographical phase retrieval algorithm for diffractive imaging*, Ultramicroscopy, 109(10), 1256-1262 (2009)

[24] https://www.synchrotron-soleil.fr/fr/lignes-de-lumiere/nanoscopium

[25] E. O. Burgos Parra, N. Bukin, M. Dupraz, G. Beutier, S. R. Sani, H. Popescu, S. A. Cavill, J. Åkerman, N. Jaouen, P. S. Keatley, R. J. Hicken, G. Van Der Laan, F. Y. Ogrin, IEEE Transactions on Magnetics, Volume PP, Issue 99 (2016).